# Northumbria Research Link

# Theoretical characterization of a non-rigid-foldable square-twist origami for property programmability

Jiayao Ma[a,b,§], Shixi Zang[a,b,§], Huijuan Feng[a,b,c], Yan Chen[a,b,*], Zhong You[b,d]

[a]Key Laboratory of Mechanism Theory and Equipment Design of Ministry of Education, Tianjin University, 135 Yaguan Road, Tianjin, 300350, China

[b]School of Mechanical Engineering, Tianjin University, 135 Yaguan Road, Tianjin, 300350, China

[c]Reconfigurable Robotics Lab, École Polytechnique Fédérale de Lausanne (EPFL), 1015 Lausanne, Switzerland

[d]Department of Engineering Science, University of Oxford, Parks Road, Oxford, OX1 3PJ, U. K.

[§] Joint first authors

**Abstract.** Using non-rigid-foldable origami patterns to design mechanical metamaterials could potentially offer more versatile behaviors than the rigid-foldable ones, but their applications are limited by the lack of analytical framework for predicting their behavior. Here, we propose a theoretical model to characterize a non-rigid-foldable square-twist origami pattern by its rigid origami counterpart. Based on the experimentally observed deformation mode the square-twist, a virtual crease was added in the central square to turn the non-rigid-foldable pattern to a rigid-foldable one. Two possible deformation paths of the non-rigid-foldable pattern were calculated through kinematic analysis of its rigid origami counterpart, and the associated energy and force were derived analytically. Using the theoretical model, we for the first time discovered that the non-rigid-foldable structure bifurcated to follow a low-energy deformation path, which was validated through experiments. Furthermore, the mechanical properties of the structure could be programmed by the geometrical parameters of the pattern and material stiffness of the creases and facets. This work thus paves the way for development of non-rigid-foldable origami-based metamaterials serving for mechanical, thermal, and other engineering applications.

**Key words**: non-rigid-foldable origami, theoretical characterization, bifurcation, programmability, mechanical metamaterials

[*] Corresponding author at: School of Mechanical Engineering, Tianjin University, Tianjin 300350, China
E-mail address: yan_chen@tju.edu.cn

## 1. Introduction

Advances in the rational design of metamaterials have enabled exotic and desirable mechanical properties that are inaccessible with conventional materials owing to their properly engineered repeating microstructures [1-14]. Origami, which transforms 2D materials into intricate 3D structures, is able to provide a geometric design approach often independent of scale and base material, and hence offers a promising platform for the design of metamaterials. The special mechanical properties that have been achieved include a negative and tunable Poisson's ratio [15, 16]; infinite stretching and bulk moduli [17]; bi- and multi-stability [18-23]; a programmable mechanical properties [24-28]; tunable stiffness and response [29, 30]; self-locking [18, 31]; shock and impact mitigation [32,33]; and superior energy and impact force absorption [34-37].

Existing origami metamaterials are predominantly developed from rigid-foldable origami patterns, represented by the well-known Miura-ori [15, 16, 35, 38-41] and its derivatives [17, 34, 36, 42] because of the simplicity of their geometric design, yet elegant kinematic property of rigid foldability with a single degree of freedom. Folding of rigid-foldable patterns is characterized by purely rotation about the creases without deformation from the facets. As a result, the folding process of a given pattern and associated rotation of each crease can be analytically derived by numerous approaches, such as the quaternions and dual quaternions [43], the matrix method [44], and kinematic theory [45]. Taking advantage of the theoretical model, the mechanical properties of the origami metamaterials can be readily predicted and further programmed by varying the geometry and the base material property [15, 18, 22, 31, 34, 35, 38]. Meanwhile, even with facet deformation during folding, non-rigid-foldable patterns can also be utilized to design origami structures and metamaterials [46]. In comparison with rigid origami, it offers a much larger collection of crease patterns, and hence could lead to wider and more versatile potential applications. However, it is very difficult to predict the motion of non-rigid-foldable origami analytically due to the simultaneous deformation along creases and within facets, and thus, developing a better and more predictive understanding on non-rigid-foldable origami remains a challenge. Overcoming this hurdle will result in novel mechanical metamaterials with programmable properties.

Here our attention is on a remarkable origami example known as the ‘square-twist’ tessellation, proposed first by Kawasaki and Yoshida [47], whose rigid foldability is decided not only by the geometry parameters but also the assignment of mountain and valley creases [48]. There are four known types of square-twist pattern with different crease assignments [49, 50], two non-rigid-foldable ones (type 1 and 2 in Fig. 1**A** and **B**) and two rigid-foldable ones (type 3 and 4 in Fig. 1**C** and **D**) [48, 51], whose rigidity is analyzed by the kinematic method based on the motion transmission path [52]. The type 1 pattern was found to have a hidden degree of freedom and bi-stability [46], which was recently employed to design origami-equivalent compliant mechanism [53], frequency reconfigurable origami antenna [54], and mechanical energy storage [55]. For the type 2 pattern, it was known that placing an additional diagonal crease on the central square facet resulted in a rigid-foldable pattern with a single degree of freedom [56], referred to as type 2M (modified type 2) hereafter in the paper (Fig. 4**A**). A mathematical model was developed to study the kinematics of the pattern with a special twist angle of 45°, from which multiple folding paths were observed [57]. In a recent study, the authors explicitly derived the kinematic equations for the generalized type 2M pattern with an arbitrary twist angle [52]. Nevertheless, little work has been published on the mechanical properties of the type 2 square-twist.

In this paper, we propose a theoretical model to investigate the mechanical properties of the non-rigid-foldable type 2 square-twist pattern and further program its properties using its rigid-foldable counterpart type 2M as a reference model. The outline of this paper is as follows. A uniaxial experiment on the type 2 pattern is presented in Section 2. In section 3 a theoretical model for the type 2 pattern is built based on kinematic analysis result of the type 2M one. The theoretical model is validated by experiments and further utilized to program the mechanical properties of the pattern in Section 4. An important bifurcation behavior of the pattern is also discussed in this section. Finally a conclusion is given in Section 5 which ends the paper.

## 2. Uniaxial tension experiment

The type 2 square-twist pattern is composed of a central square facet, four trapezoidal ones and four rectangular ones, with the mountain-valley crease arrangement and folded configuration shown in Fig. 1**B**. It is parameterized by two side lengths, $l$ and $a$, and a twist angle, $\alpha$. For theoretical characterization of the non-rigid-foldable pattern, determination of the deformation mode is a prerequisite. Folding and unfolding of a cardboard model indicated that besides rotation of the creases, the central square seemed to be noticeably bent whereas all the other facets were nearly flat. To quantify the deformation of the central square, a uniaxial tension experiment in the diagonal direction was conducted on a type 2 specimen. The experimental setup is shown in Fig. 2**A**. The experiment was conducted on a horizontal testing machine developed in house to avoid the influence of gravity. The machine had a load cell of 50N with an accuracy of 0.5% and a stroke of 80mm. The specimen was attached to the machine using two fixtures. The left one was fixed on the load cell, whereas the right one on a support had a rotational degree of freedom to allow the specimen to rotate about the $x$ axis. Moreover, a hinge was connected to each fixture to enable rotation of the specimen about the $y$ axis. The specimen was tensioned by a displacement of 32.96mm at the loading rate of 0.2mm/s to eliminate dynamic effects. The deformation process of the experiments was recorded using a standard digital camera (Canon 70D) at 25 frames per second. The exact deformed configuration of the central square facet was captured by a digital image correlation (DIC) system CSI Vic-3D9M with a camera resolution of 2704×3384 pixels at a frame time interval of 500ms.

The specimen shown in Fig. 2**B** was fabricated from polyethylene terephthalate (PET) of thickness $t$=0.5mm using a Trotec Speedy 300 laser cutter. The geometry of the specimen was selected as $a$=25mm, $l$=25mm, and $\alpha$=30º. The creases were cut as dotted lines of 2mm perforations at 1mm intervals and then folded by hand to form the origami structure. The central square was painted with black speckles for DIC capture.

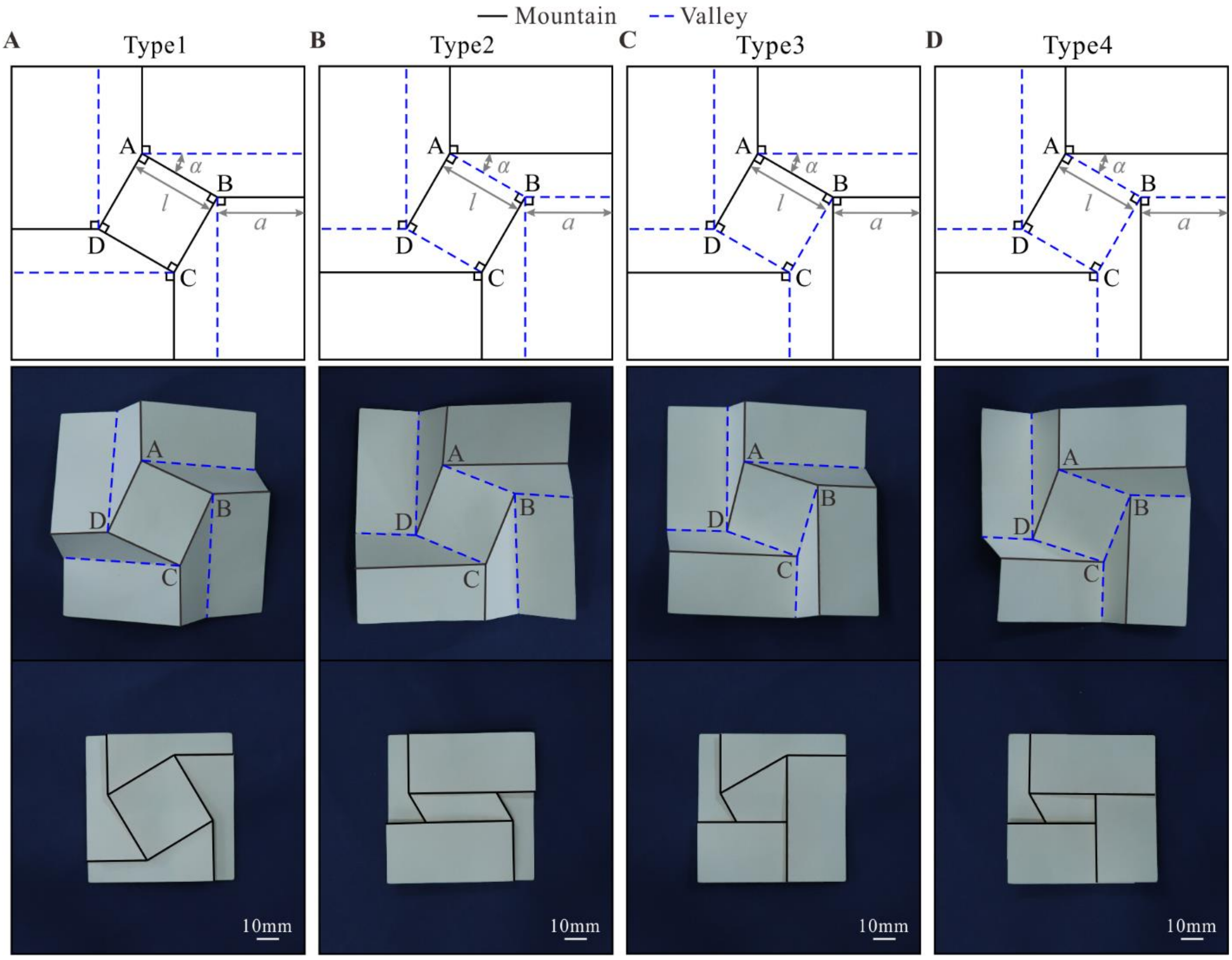


**Fig. 1.** Crease arrangements, geometric parameters, deployed and folded configurations of (A) type 1, (B) type 2, (C) type 3, and (D) type 4 square-twist units, where side lengths $a$=25mm, $l$=25mm, and twist angle $\alpha$=30º. The mountain and valley creases are described by black and blue dotted lines, respectively.

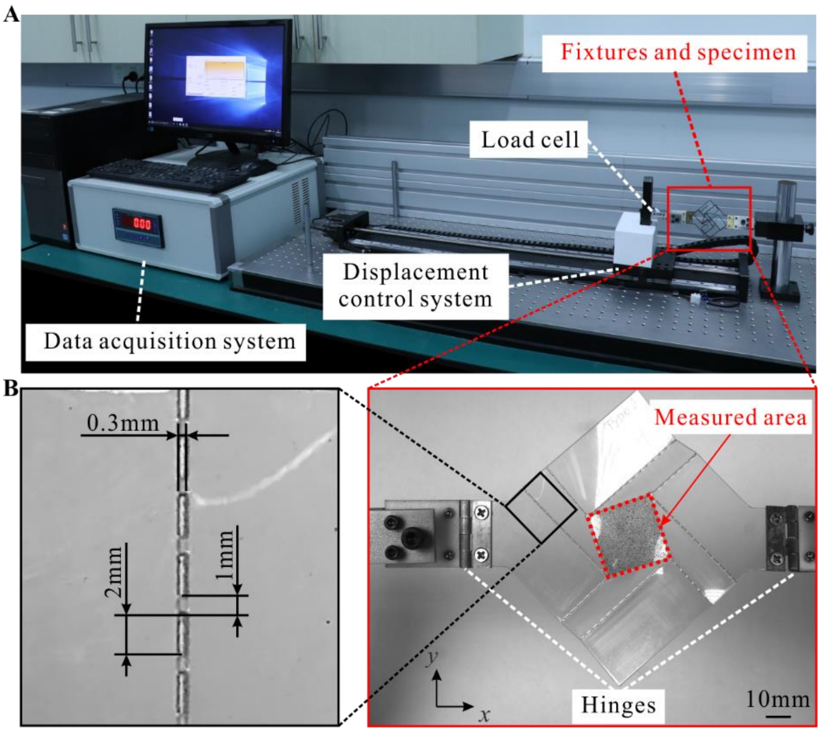


**Fig. 2.** Uniaxial tension experiment. (**A**) Experimental setup. The horizontal testing machine consists of a load cell, displacement control, and data acquisition systems. (**B**) Details of the specimen and fixtures. The creases were cut as 2mm×0.3mm perforations at 1mm intervals. The specimen, whose measured area was marked by red lines, was connected to the two fixtures by hinges.

The experimental result of the type 2 specimen is shown in Fig. 3. Four configurations of the specimen with tension displacement $\Delta x$=0mm, 4.84mm, 15.48mm, and 21.12mm, are shown in Fig. 3**A** as representatives. It is observed that during tension, facet rotation about the creases dominates, whilst the central square facet always bends and unbends along diagonal A–C (also in Supplementary Video S1). Then the exposed areas of the square enclosed in the red quadrilateral regions are geometrically reconstructed using DIC and subsequently fit it with single-curved surfaces with the following polynomial governing equations

$$f_{\mathrm{I}}(x)=0 \tag{1a}$$

$$f_{\mathrm{II}}(x)=-1.61\times10^{-6}x^4-3.23\times10^{-5}x^3+1.11\times10^{-2}x^2+1.76\times10^{-2}x-3.72\times10^{-2} \tag{1b}$$

$$f_{\mathrm{III}}(x)=2.26\times10^{-6}x^4-3.16\times10^{-5}x^3+1.36\times10^{-2}x^2-1.47\times10^{-2}x-3.61\times10^{-1} \tag{1c}$$

$$f_{\mathrm{IV}}(x)=5.36\times10^{-6}x^4-2.00\times10^{-5}x^3+1.17\times10^{-2}x^2-8.10\times10^{-3}x-3.06\times10^{-1} \tag{1d}$$

As shown in Fig. 3**B**, a good match between the experimental result and fitting surface is obtained in all four configurations, with the fitting error calculated in Fig. 3**C** being within half of the material thickness in over 90% of the measured area. Hence, we have proven experimentally that the central square of the type 2 pattern is subjected to bending with a single curvature, based on which we will build a theoretical model to characterize its mechanical behavior.

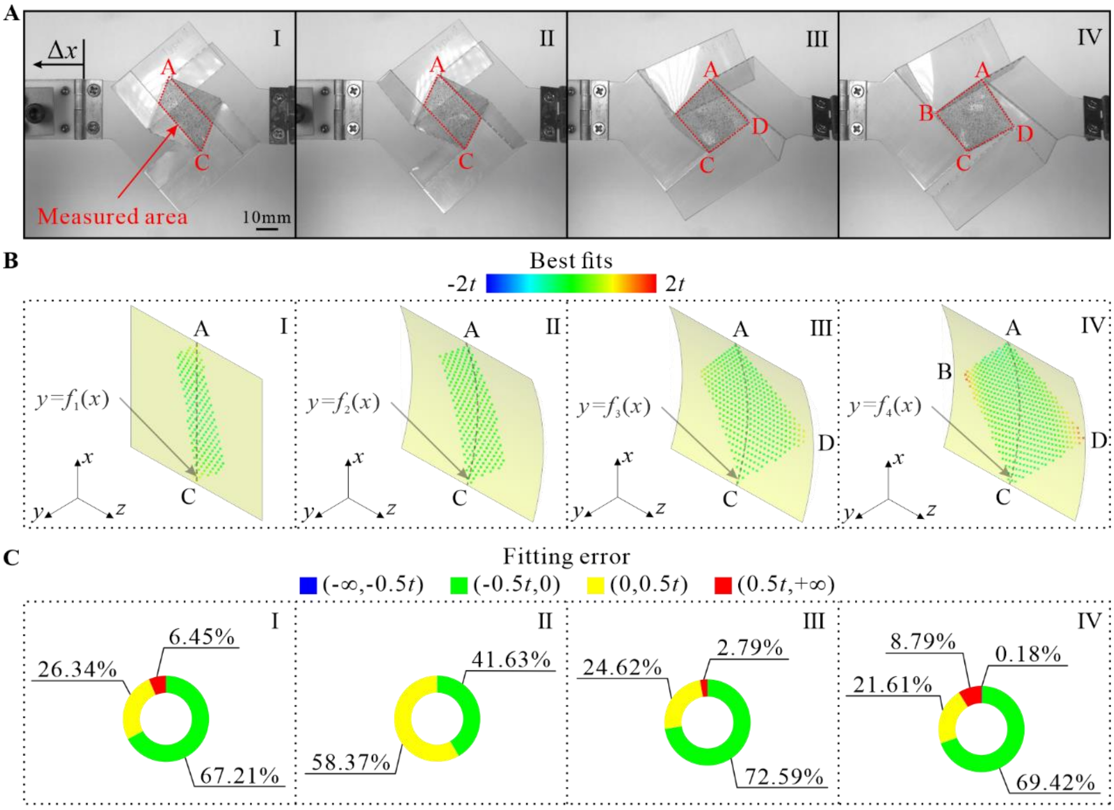


**Fig. 3.** Reconstructed central squares (measured area) using digital image correlation. (**A**) Configuration of the specimen at four representative tension displacements. The central square was painted with speckles for DIC and the exposed area of the square enclosed in the red quadrilateral region was captured. (**B**) Geometrically reconstructed central squares (measured area) using DIC and best-fit polynomial single-curved surfaces (Eq. 1). (**C**) The pie graphs of the errors between the experimental results and fitting surfaces indicate that in all four configurations, the fit error is within half of the material thickness, t, in over 90% of the measured area.

## 3. Theoretical modelling

As mentioned in the Introduction, deformation of origami structures made of rigid-foldable patterns comes only from rotation of creases, the dihedral angles of which can be theoretically derived. Consequently, the elastic energy of the structure can be easily calculated by adding up the energy in each crease [16]. For theoretical characterization of the non-rigid-foldable type 2 pattern, however, two major challenges arise, i.e., how to obtain the dihedral angles of the creases and how to calculate the bending energy of the deformed central square. The existing simulations for deformable facets are using bar-and-hinge models [58] or pin-jointed bar framework models [59] to provide an approximation for the bending behavior. Here, we adopt the approach adding a virtual diagonal crease between vertices B and D on the central square so as to derive the dihedral angles of all the creases from the kinematic model of the type 2M pattern in Fig. 4**A**, and to quantify the bending energy of the central square as rotation energy of the virtual crease.

Taking the notations as shown in Fig. 4**A**, the dihedral angles of all the 13 creases, as well as the diagonal tension displacement, can be determined by only one input dihedral angle, which is set as $\varphi_4$, from the kinematic model recently developed by the authors [52] (detailed mathematical equations in Supplementary Section 1). The kinematic research in ref [52] shows that arbitrary $\varphi_4$ corresponds to one $\varphi_i$ ($i$=1, 2, 3, 7, 8, 9, 10) and two different values of $\varphi_j$ ($j$=5, 6, 11, 12, 13), which implies that there are two kinematic paths between the fully folded and deployed configurations of type 2M pattern. The kinematic relationship of $\varphi_6$ and $\varphi_4$ is drawn in Fig. 4**B**, together with six representative configurations I-VI during unfolding. The two distinct paths of the kinematic model are bifurcated at the point in red where $\varphi_4=\varphi_6=105.54^{\circ}$ (configurations IV$_1$ and IV$_2$). However, we observe penetration of the facets on kinematic path 2 between the fully folded and bifurcation configurations, which is exemplified by configuration II$_2$ in Fig. 4**B**. This is important as it implies that when the pattern is unfolded, it may not be able to follow kinematic path 2 because of physical interference. Hence, there are two kinematically admissible paths to unfold it: one is path 1 throughout, and the other is path 1 first, followed by a switch to path 2 at the point where the paths bifurcate.

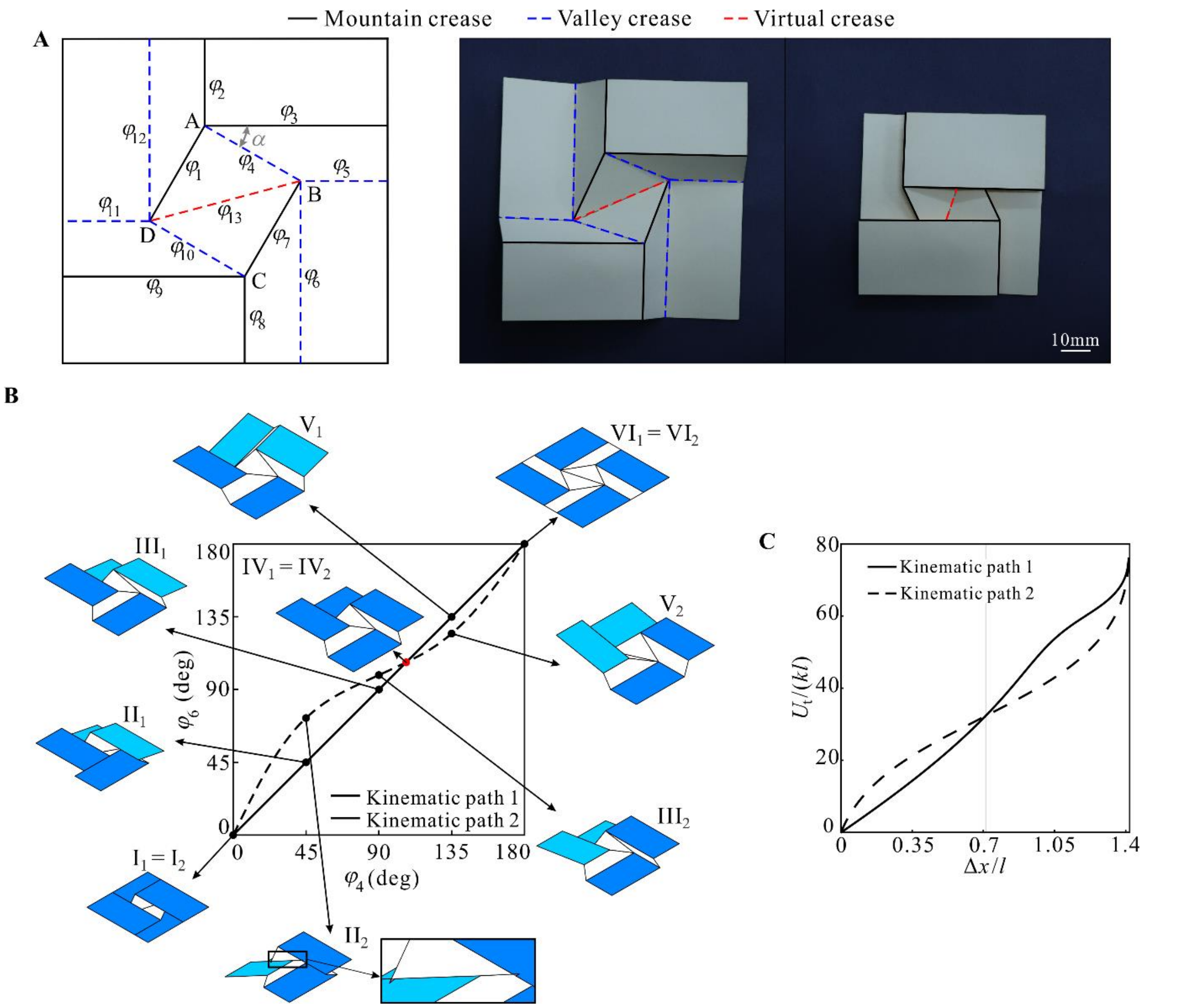


**Fig. 4.** Kinematics and theoretical energy of the type 2M unit. (**A**) Crease arrangement, notation of dihedral angles, and the folded and deployed configurations of the type 2M pattern. The mountain, valley, and virtual creases are described by black, blue dotted and red dotted lines, respectively. (**B**) Two different kinematic paths of the type 2M pattern together with six representative configurations on each path. The configurations ($\mathrm{I}_1$ $\mathrm{II}_1$ $\mathrm{III}_1$ $\mathrm{IV}_1$ $\mathrm{V}_1$ $\mathrm{VI}_1$) represent the unfolding sequence on path 1; ($\mathrm{I}_2$ $\mathrm{II}_2$ $\mathrm{III}_2$ $\mathrm{IV}_2$ $\mathrm{V}_2$ $\mathrm{VI}_2$) represent the unfolding motion on path 2. Rectangular facets in the same colour (dark or light blue) are parallel during motion. (**C**) Normalized theoretical elastic energy $U_t/kl$ vs. $\varphi_4$ of the type 2M pattern.

Using the dihedral angles determined above, the elastic energy, $U_t$, of the type 2 pattern during unfolding along either kinematic path can be calculated as the summation of the energy of the twelve original creases, $U_c$, and that of the virtual crease on the central square, $U_s$.

$$U_t = U_c + U_s = \frac{1}{2}\sum_{i=1}^{12} k_i \cdot L_i \left(\varphi_i - \varphi_{i,0}\right)^2 + \frac{1}{2} k' \cdot L_s \left(\varphi_s - \varphi_{s,0}\right)^2 \tag{2}$$

In which $k_i$, $L_i$, $\varphi_i$ and $\varphi_{i,0}$ are, respectively, the torsional elastic constant per unit length along the crease, length of the crease, dihedral angle and natural dihedral angle in the undeformed state for the

$i$-th crease, whilst $k'$, $L_s$, $\varphi_s$ and $\varphi_{s,0}$ are the corresponding parameters of the virtual crease. Using equation (2), the elastic energy of a type 2 pattern following each kinematic path is calculated, normalized by $kl$, and drawn against normalized tension displacement $\Delta x/l$ in Fig. 4**C** (detailed derivation in Supplementary Section 1). The geometry of the pattern is selected as $\alpha$=30°, $a$=$l$, $\varphi_{4,0}$=0°, and the ratio $k'/k$ is set to 8 in order to exemplify the difference between the two paths. It can be seen that the elastic energy of kinematic path 2 is higher than that of path 1 prior to the bifurcation point and becomes lower than that of path 1 afterward. Theoretically, when a structure is loaded, the low-energy deformation path will be followed. Therefore, the theoretical model predicts that the type 2 pattern will initially follow path 1 and then bifurcate to follow path 2, which has not been reported in origami structures of its kind.

It is worth mentioning that equation (2) is valid only when the creases have a linear elastic torque versus rotation angle relationship, and modifications are required should a different constitutive relationship be adopted.

# 4. Results and discussions

## 4.1 Validation of the theoretical model

To validate the theoretical model derived in Section 3, we first built and tested a rigid-foldable type 2M specimen. The specimen had identical geometric parameters with the type 2 one in Fig. 3**A** except for the additional crease at the central square, and was manufactured and tensioned in the same manner. The experimental results are presented in Fig. 5**A** (deformation process in Supplementary Video S2). The force is measured directly from the experiment and the energy is obtained by integration of the force over the displacement.

Then the theoretical total energy of the specimen following the two kinematic paths are calculated and differentiated with respect to tension displacement to obtain force. In the calculation, the natural dihedral angle $\varphi_{4,0}$=40º is measured from the specimen, whereas the others are derived based on the kinematic model. An elastic-perfectly plastic model is found to be able to realistically model the relationship between crease torque and rotation angle. The torsional elastic constant and yield rotation angle are determined as $k$=$k'$=0.76N·rad$^{-1}$ and $\Delta\varphi_y$=15.23º based on experiment and curve fitting (Supplementary Section 2). Correspondingly, equation (2) is modified as follows to calculate the total energy of the type 2M specimen

$$U_t = \sum_{i=1}^{13} k \cdot L_i \left[ \frac{1}{2} \Delta\varphi_y^{\ 2} + \Delta\varphi_y \left( \varphi_i - \varphi_{i,0} - \Delta\varphi_y \right) \right] \tag{3}$$

The theoretically derived normalized total energy, $U_t/(kl)$, and normalized force, $F/k$, are drawn against normalized displacement $\Delta x/l$ in together with the experimental ones in Fig. 5**A**. Note that before the bifurcation point, only the energy and force on kinematic path 1 are calculated, because kinematic path 2 in this range is inaccessible in experiments owing to physical interference. As expected, the experimental curves bifurcate and follow the low-energy deformation path throughout loading. One discrepancy, however, is that the tiny force drops at bifurcation point in the theoretical curve is not observed in the experimental curve, possibly because the magnitude of the force drop is too small.

Subsequently we validate the model by comparing the experimental and theoretical results for the non-rigid-foldable type 2 specimen in Fig. 3**A** with a natural dihedral angle of $\varphi_{4,0}$=30º. The same procedure as in the case of the type 2M pattern is followed expect for that the torsional stiffness of the virtual crease needs to be determined. According to the digital image correlation result, the central square remains elastic during loading, and therefore the virtual crease is deemed linear elastic with a torsional constant $k'$=1.11N·rad$^{-1}$ calculated based on the bending stiffness of the central square (Supplementary Section 2). Consequently, the theoretical total energy can be calculated by modification of equation (2) as follows

$$U_{\mathrm{t}}=\sum_{i=1}^{12}k\cdot L_i\left[\frac{1}{2}\Delta\varphi_{\mathrm{y}}{}^2+\Delta\varphi_{\mathrm{y}}\left(\varphi_i-\varphi_{i,0}-\Delta\varphi_{\mathrm{y}}\right)\right]+\frac{1}{2}k'\cdot L_{\mathrm{s}}\left(\varphi_{\mathrm{s}}-\varphi_{\mathrm{s},0}\right)^2 \tag{5}$$

Then the force can also be derived by differentiation of the energy against displacement.

The theoretical and experimental results are presented in Fig. 5**B**. Again a reasonable agreement is achieved, especially with respect to the four feature points I–IV on the force curve. In addition, the theoretical force reaches a local maximum (point III) at the bifurcation point and then drops. This is because the virtual diagonal crease starts to unbend when the structure reaches its bifurcation configuration, which releases elastic energy and causes a drop in the force. Notice that the drop is not as dramatic in the experiment due to that the limited rigidity of the facets makes them deform simultaneously with the creases. Therefore, we can conclude that we have solved the two challenges for theoretical characterization of the non-rigid-foldable pattern. Our analytical model, which combines kinematics and mechanics, can accurately predict the mechanical behaviors of the type 2 square-twist pattern.

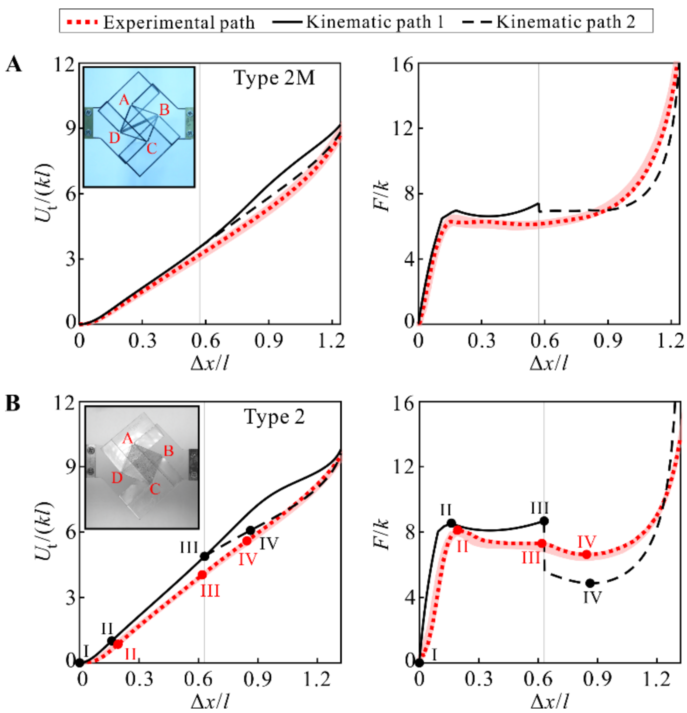


**Fig. 5.** Theoretical and experimental normalized energy $U_t/(kl)$ and normalized force $F/k$ versus normalized displacement $\Delta x/l$ for (**A**) the type 2M specimen with the natural dihedral angle $\varphi_{4,0}$=40º, and (**B**) the type 2 specimen with the natural dihedral angle $\varphi_{4,0}$=30º. Bifurcation of the theoretical

curves occurs at $\varphi_{13}$=94.12°. Note that the natural dihedral angle of the unloaded physical specimen is affected by the pattern adopted; therefore, the type 2M and 2 specimens have different values for $\Delta x/l$. The red shade described the repeatability of the experimental results of several specimens.

### 4.2 Stability of deformation path

It has been shown that if undisturbed during loading, both type 2M and type 2 patterns will follow the low-energy path. However, it would be interesting to know if initially placed on the high energy path, whether it will follow it or drop to the low-energy one. To investigate this, we fabricated a type 2M specimen with two voids of 9.50mm by 16.50mm (inset of Fig. 6) to eliminate physical interferences. This made the branch of kinematic path 2 before bifurcation point physically reachable, leading to four possible deformation modes: path 1 throughout deformation; path 1 followed by path 2; path 2 followed by path 1, and path 2 throughout. Then four experiments were conducted on the specimen, and the experimental paths in terms of $\varphi_6$ versus $\varphi_4$ were measured and presented in Fig. 6. Specifically, in experiment 1, the specimen was set initially on kinematic path 1 and tensioned without disturbance. It moved on path 1 up to the bifurcation point and then dropped to kinematic path 2. In experiment 2, the specimen was also on kinematic path 1 initially. Immediately after it bifurcated to path 2, we manually adjusted it back to kinematic path 1 and then applied further tension. However, the specimen did not stay on kinematic path 1 and quickly dropped to kinematic path 2. Experiments 3 and 4 respectively followed the procedures of experiments 1 and 2, but started from a configuration on kinematic path 2. In both cases, the specimen quickly dropped to the low-energy path (i.e., path 1 prior to and path 2 after the bifurcation point). Those experimental findings agree with theoretical analysis. Moreover, the results imply that the origami structure will follow a stable deformation path that is insensitive to perturbation, which make it better adaptive to various work conditions.

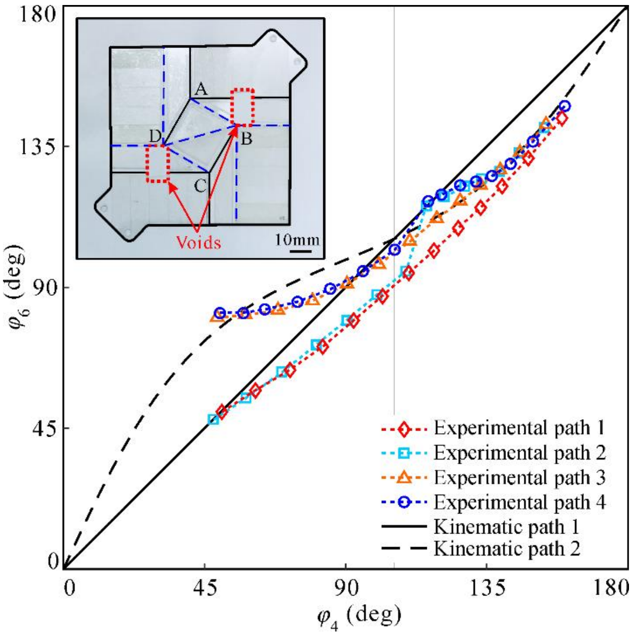


**Fig. 6.** Two kinematic paths and four experimental paths of a type 2M specimen with two voids. In the experiments, the initial dihedral angle $\varphi_{4,0}$=45º.

## 4.3 Programmability of the type 2 pattern

Using our theoretical model, we can readily program the mechanical response of the type 2 pattern by simply changing the material and geometrical parameters. This is demonstrated by calculating and comparing the energy and force of a series of structures with varying parameters. In the calculation, the same elastic-perfectly plastic original creases, linear elastic virtual crease, and natural dihedral angle $\varphi_{4,0}$=30º as those for the type 2 specimen in Fig. 3**A** are adopted. And the displacement is normalized by the maximum displacement, $\Delta x_{max}$, in all the curves for convenient comparison. The material parameter that we investigate is the ratio of the torsional stiffness of the virtual crease, which is essentially the bending stiffness of the central square, to that of the original creases. The energy and force curves of five models with identical $\alpha$=30º and $a/l$=1, but different $k'/k$ values ranging from 1 to 16, are presented in Fig. 7**A**. It can be seen that as the ratio increases, both the energy and force increase. This is because at higher torsional stiffness, more energy is required to deform the central square, thereby lifting the force barrier to reach bifurcation. Furthermore, the decrease in force at the bifurcation point becomes larger, and a negative force occurs when $k'/k$ surpasses 5.04. The condition for the existence of a negative force is analyzed in Supplementary Section 3. Briefly, this phenomenon is best explained by the variation in the bending energy of the central square. It has been shown in

Fig. 5**B** that the unbending of the central square after bifurcation releases elastic energy and leads to a drop in the force. As shown in the second diagram of Fig. 7**A**, the ratio of the central square bending energy to the crease energy, $U_s/U_c$, increases with $k'/k$. When $k'/k>5.04$, the energy release in the central square is greater than the energy increase in the original creases, leading to a reduction in the total energy of the structure and a corresponding negative force. Therefore, the mechanical properties and behavior of the structure can be programmed simply by tuning the bending stiffness of the central square facet.

The geometric parameters also influence the behavior of the structure. A comparison of five models with $\alpha$ in the range of $25^\circ$–$45^\circ$, $k'/k=1$ and $a/l=1$ indicates that increasing the twist angle lowers the initial peak force but raises the force barrier to the bifurcation point (Fig. 7**B**). Decreasing $a/l$, which means keeping the size of the central square constant while shortening the facets around it, reduces the entire force level owing to the decrease in the crease lengths, see the results in Fig. 7**C** from five models with $a/l$ ranging from 1/4 to 4 while $\alpha=30^\circ$ and $k'/k=1$. The force drop in the bifurcation point becomes more pronounced with decreasing $a/l$ because of the higher bending energy of the central square facet.

This programmability through the pattern geometry and material allows various mechanical functions to be achieved in the origami structure. For example, to design an ideal impact energy absorption device, which requires a long and flat plateau [60], smaller values of $k'/k$ and $\alpha$, and larger value of $a/l$ should be selected to minimize the force drop at the bifurcation point. The third diagram shown in Fig. 7**C** shows nearly perfect force plateaus when $k'/k=1$ and $\alpha=30^\circ$. The height of the plateaus increases with the ratio $a/l$.

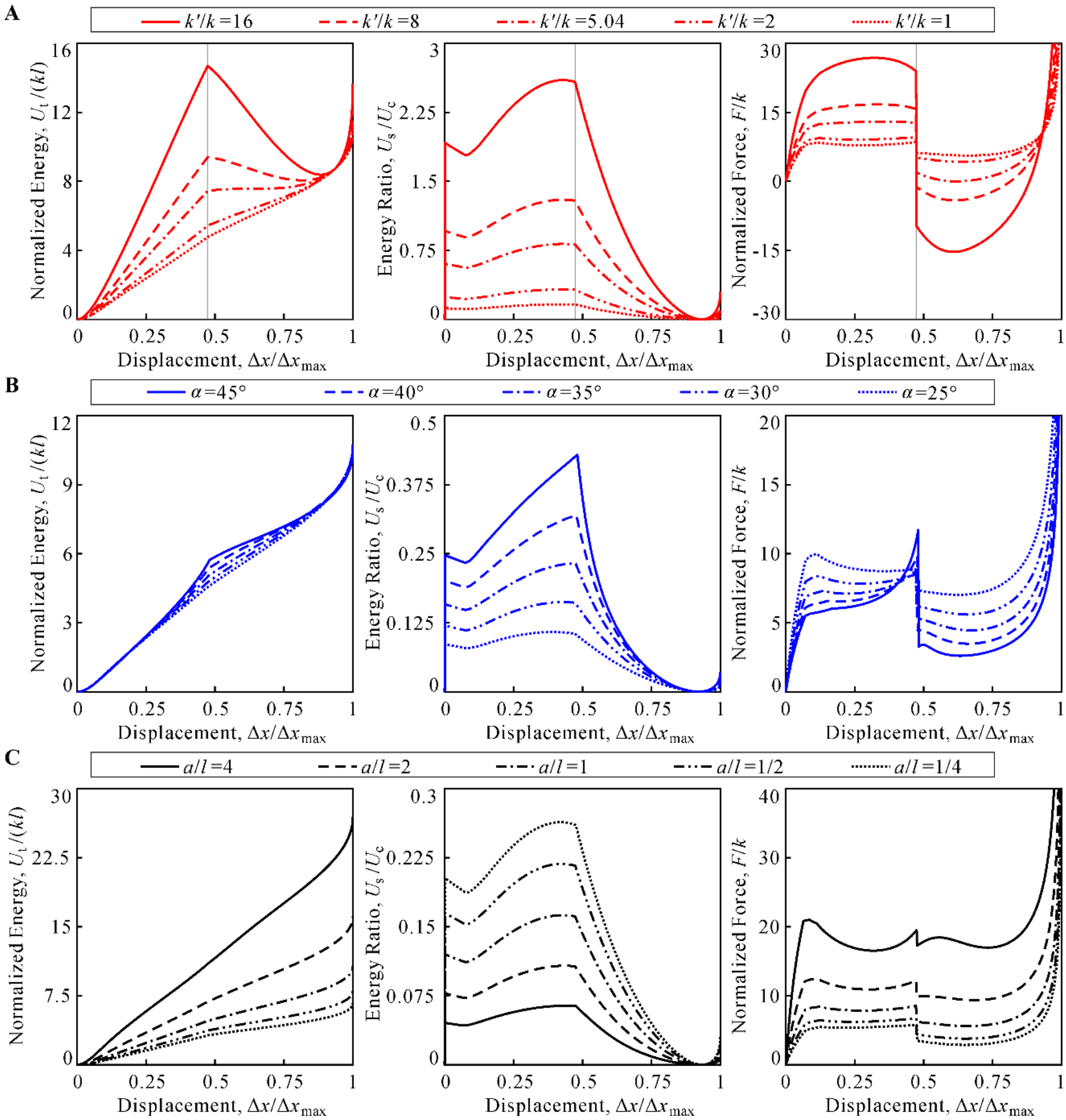


**Fig. 7.** The effects of (**A**) the stiffness ratio $k'/k$, (**B**) the twist angle $\alpha$, and (**C**) the side length ratio $a/l$ on the mechanical properties of the type 2 pattern derived from the theoretical model. The normalized energy, $U_t/(kl)$, ratio of the central square bending energy to the crease energy, $U_s/U_c$, and normalized force, $F/k$, were calculated from the theoretical model of Eq. 5, where $k$ is the torsional elastic constant of the elastic-perfectly plastic original creases, and $k'$ is the torsional elastic constant of the elastic virtual crease. The normalized displacement, $\Delta x/\Delta x_{max}$, of the bifurcation is equal to 0.47 in (A), ranges from 0.47 to 0.48 in (B), and have a minimum value of 0.47 when $a=l$ in (C).

## 5. Conclusion

In conclusion, we have developed a theoretical model for a non-rigid-foldable square-twist pattern to achieve predictable programmable mechanical behavior, based on the kinematic analysis results of its rigid-foldable counterpart. We have demonstrated theoretically and experimentally that the non-rigid-foldable pattern bifurcates during tension so as to always follow the low-energy path. This feature has not been reported previously for origami structures. With the model, we are also able to accurately program the mechanical properties of the origami structure by tuning the geometry of the pattern and/or mechanical properties of the creases and the central square facet. Altogether, this work enables the use of non-rigid-foldable origami patterns in the design of mechanical metamaterials with theoretically predictive behavior.

Based on the approach we proposed here, for the general non-rigid origami pattern, it is possible to find its rigid counterpart by introducing virtual creases. Yet, there is no ready solution for every non-rigid pattern. Kinematic and mechanical experiments and analysis have to be conducted case by case to allocate the virtual creases. For complicated patterns, there could be multiple choices for the virtual creases corresponding to different base materials and boundary conditions. Next, we will extend the type 2 square-twist studied here to metamaterials with combination of square-twist pattern of different types. The properties of metamaterials will be programmed by tuning the units in whole or individually, which will offer a platform to achieve metamaterials with variable properties in much wider regions.

## Acknowledgements

Y. C. acknowledges the support of the National Natural Science Foundation of China (Projects 51825503, 51721003), J. M. acknowledges the support of the National Natural Science Foundation of China (Projects 51575377), and Z. Y. acknowledges the support of the Air Force Office of Scientific Research (FA9550-16-1-0339).

## References

[1] Bertoldi K, Reis PM, Willshaw S, Mullin T. Negative Poisson's ratio behaviour induced by an elastic instability. Adv Mater 2010; 22: 361-366. https://doi.org/10.1002/adma.200901956.

[2] Chen Y, Li T, Scarpa F, Wang L. Lattice metamaterials with mechanically tunable Poisson's ratio for vibration control. Phys Rev Applied 2017; 7: 024012. https://doi.org/10.1103/PhysRevApplied.7.024012.

[3] Zheng X, Lee H, Weisgraber TH, Shusteff M, DeOtte J, Duoss EB, Kuntz JD, Biener MM, Ge Q, Jackson JA, S. O. Kucheyev, N. X. Fang, C. M. Spadaccini. Ultralight, ultrastiff mechanical metamaterials. Science 2014; 344: 1373-1377. https://doi.org/10.1126/science.1252291.

[4] Coulais C, Sounas D, Alù A. Static non-reciprocity in mechanical metamaterials. Nature 2017; 542: 461-464. https://doi.org/10.1038/nature21044.

[5] Lee JH, Wang L, Boyce MC, Thomas EL. Periodic bicontinuous composites for high specific energy absorption. Nano Lett 2012; 12: 4392-4396. https://doi.org/10.1021/nl302234f.

[6] Frenzel T, Kadic M, Wegener M. Three-dimensional mechanical metamaterials with a twist. Science 2017; 358: 1072-1074. https://doi.org/10.1126/science.aao4640.

[7] Coulais C, Kettenis C, van Hecke M. A characteristic length scale causes anomalous size effects and boundary programmability in mechanical metamaterials. Nat Phys 2018; 14: 40-44. https://doi.org/10.1038/nphys4269.

[8] Wang H, Zhang Y, Lin W, Qin QH. A novel two-dimensional mechanical metamaterial with negative Poisson's ratio. Comp Mater Sci 2020; 171: 109232. https://doi.org/10.1016/j.commatsci.2019.109232.

[9] Pan F, Li Y, Li Z, Yang J, Liu B, Chen Y. 3D pixel mechanical metamaterials. Adv Mater 2019; 31: 1900548. https://doi.org/10.1002/adma.201900548.

[10] Zhong R, Fu M, Chen X, Zheng B, Hu L. A novel three-dimensional mechanical metamaterial with compression-torsion properties. Compos Struct 2019; 226: 111232. https://doi.org/10.1016/j.compstruct.2019.111232.

[11] Coulais C, Sabbadini A, Vink F, van Hecke M. Multi-step self-guided pathways for shape-changing metamaterials. Nature 2018; 561: 512-515. https://doi.org/10.1038/s41586-018-0541-0.

[12] Liu K, Zegard T, Pratapa PP, Paulino GH. Unraveling tensegrity tessellations for metamaterials with tunable stiffness and bandgaps. J Mech Phys Solids 2019; 131: 147-166. https://doi.org/10.1016/j.jmps.2019.05.006.

[13] Zhang W, Zhao S, Sun R, Scarpa F, Wang J. In-plane mechanical behavior of a new star-re-entrant hierarchical metamaterial. Polymers 2019; 11: 1132. https://doi.org/10.3390/polym11071132.

[14] Zhang Y, Li B, Zheng QS, Genin GM, Chen CQ. Programmable and robust static topological solitons in mechanical metamaterials. Nat Commun 2019; 10: 1-8. https://doi.org/10.1038/s41467-019-13546-y.

[15] Schenk M, Guest SD. Geometry of Miura-folded metamaterials. Proc Natl Acad Sci USA 2013; 110: 3276-3281. https://doi.org/10.1073/pnas.1217998110.

[16] Wei ZY, Guo ZV, Dudte L, Liang HY, Mahadevan L. Geometric mechanics of periodic pleated origami. Phys Rev Lett 2013; 110: 215501. https://doi.org/10.1103/PhysRevLett.110.215501.

[17] Zhou X, Zang S, You Z. Origami mechanical metamaterials based on the Miura-derivative fold patterns. Proc R Soc A 2016; 472: 20160361. https://doi.org/10.1098/rspa.2016.0361.

[18] Kamrava S, Mousanezhad D, Ebrahimi H, Ghosh R, Vaziri A. Origami-based cellular metamaterial with auxetic, bistable, and self-locking properties. Sci Rep 2017; 7: 46046. https://doi.org/10.1038/srep46046.

[19] Waitukaitis S, Menaut R, Chen BGG, van Hecke M. Origami multistability: From single vertices to metasheets. Phys Rev Lett 2015; 114: 055503. https://doi.org/10.1103/PhysRevLett.114.055503.

[20] Li S, Wang KW. Fluidic origami with embedded pressure dependent multi-stability: a plant inspired innovation. J R Soc Interface 2015; 12: 20150639. https://doi.org/10.1098/rsif.2015.0639.

[21] Brunck V, Lechenault F, Reid A, Adda-Bedia M. Elastic theory of origami-based metamaterials. Phys Rev E 2016; 93: 033005. https://doi.org/10.1103/PhysRevE.93.033005.

[22] Fang H, Chang T, Wang KW. Magneto-origami structures: engineering multi-stability and dynamics via magnetic-elastic coupling. Smart Mater Struct 2020; 29: 015026. https://doi.org/10.1088/1361-665X/ab524e.

[23] Sengupta S, Li S. Harnessing the anisotropic multistability of stacked-origami mechanical metamaterials for effective modulus programming. J Intel Mat Syst Str 2018; 29: 2933-2945. https://doi.org/10.1177/1045389X18781040.

[24] Silverberg JL, Evans AA, McLeod L, Hayward RC, Hull T, Santangelo CD, Cohen I. Using origami design principles to fold reprogrammable mechanical metamaterials. Science 2014; 345: 647–650. https://doi.org/10.1126/science.1252876.

[25] Tang Y, Li Y, Hong Y, Yang S, Yin J. Programmable active kirigami metasheets with more freedom of actuation. Proc Natl Acad Sci USA 2019; 116: 26407-26413. https://doi.org/10.1073/pnas.1906435116.

[26] Yang N, Zhang M, Zhu R, Niu XD. Modular metamaterials composed of foldable obelisk-like units with reprogrammable mechanical behaviors based on multistability. Sci Rep 2019; 9: 1-7. https://doi.org/10.1038/s41598-019-55222-7.

[27] He YL, Zhang PW, You Z, Li ZQ, Wang ZH, Shu XF. Programming mechanical metamaterials using origami tessellations. Compos Sci Technol 2020; 108015. https://doi.org/10.1016/j.compscitech.2020.108015.

[28] Kamrava S, Ghosh R, Wang Z, Vaziri A. Origami-inspired cellular metamaterial with anisotropic multi-stability. Adv Eng Mater 2019; 21: 1800895. https://doi.org/10.1002/adem.201800895.

[29] Zhai Z, Wang Y, Jiang H. Origami-inspired, on-demand deployable and collapsible mechanical metamaterials with tunable stiffness. Proc Natl Acad Sci USA 2018; 115: 2032-2037. https://doi.org/10.1073/pnas.1720171115.

[30] Reid A, Lechenault F, Rica S, Adda-Bedia M. Geometry and design of origami bellows with tunable response. Phys Rev E 2017; 95: 013002. https://doi.org/10.1103/PhysRevE.95.013002.

[31] Fang H, Chu SCA, Xia Y, Wang KW. Programmable self-locking origami mechanical metamaterials. Adv Mater 2018; 30: 1706311. https://doi.org/10.1002/adma.201706311.

[32] Yasuda H, Chong C, Charalampidis EG, Kevrekidis PG, Yang J. Formation of rarefaction waves in origami-based metamaterials. Phys Rev E 2016; 93: 043004. https://doi.org/10.1103/PhysRevE.93.043004.

[33] Yasuda H, Miyazawa Y, Charalampidis EG, Chong C, Kevrekidis PG, Yang J. Origami-based impact mitigation via rarefaction solitary wave creation. Sci Adv 2019; 5: eaau2835. https://doi.org/10.1126/sciadv.aau2835.

[34] Ma J, Song J, Chen Y. An origami-inspired structure with graded stiffness. Int J Mech Sci 2018; 136: 134-142. https://doi.org/10.1016/j.ijmecsci.2017.12.026.

[35] Zhang J, Karagiozova D, You Z, Chen Y, Lu G. Quasi-static large deformation compressive behaviour of origami-based metamaterials. Int J Mech Sci 2019; 153: 194-207. https://doi.org/10.1016/j.ijmecsci.2019.01.044.

[36] Yuan L, Dai H, Song J, Ma J, Chen Y. The behavior of a functionally graded origami structure subjected to quasi-static compression. Mater Design 2020; 189: 108494. https://doi.org/10.1016/j.matdes.2020.108494.

[37] Wickeler A, Naguib HE. Novel origami-inspired metamaterials: Design, mechanical testing and finite element modelling. Mater Design 2020; 186: 108242. https://doi.org/10.1016/j.matdes.2019.108242.

[38] Lv C, Krishnaraju D, Konjevod G, Yu HY, Jiang HQ. Origami based mechanical metamaterials. Sci Rep 2014; 4: 5979. https://doi.org/10.1038/srep05979.

[39] Wang Z, Jing L, Yao K, Yang Y, Zheng B, Soukoulis CM, Chen H, Liu Y. Origami-based reconfigurable metamaterials for tunable chirality. Adv Mater 2017; 29: 1700412. https://doi.org/10.1002/adma.201700412.

[40] Nauroze SA, Novelino LS, Tentzeris MM, Paulino GH. Continuous-range tunable multilayer frequency-selective surfaces using origami and inkjet printing. Proc Natl Acad Sci USA 2018; 115: 13210-13215. https://doi.org/10.1073/pnas.1812486115.

[41] Boatti E, Vasios N, Bertoldi K. Origami metamaterials for tunable thermal expansion. Adv Mater 2017; 29: 1700360. https://doi.org/10.1002/adma.201700360

[42] Eidini M, Paulino GH. Unraveling metamaterial properties in zigzag-base folded sheets. Sci Adv 2015; 1: e1500224. https://doi.org/10.1126/sciadv.1500224.

[43] Wu W, You Z. Modelling rigid origami with quaternions and dual quaternions. Proc R Soc A 2010; 466: 2155-2174. https://doi:10.1098/rspa.2009.0625.

[44] Watanabe N, Kawaguchi KI. The method for judging rigid foldability. In Origami 4 (eds Lang RJ); 2009, pp. 165-174. Natick, MA: A. K. Peters.

[45] Stachel H. A kinematic approach to Kokotsakis meshes. Comput Aided Geom Des 2010; 27: 428-437. https://doi: 10.1016/j.cagd.2010.05.002.

[46] Silverberg JL, Na JH, Evans AA, Liu B, Hull TC, Santangelo CD, Lang RJ, Hayward RC, Cohen I. Origami structures with a critical transition to bistability arising from hidden degrees of freedom. Nat Mater 2015; 14: 389-393. https://doi.org/10.1038/nmat4232.

[47] Kawasaki T, Yoshida M. Crystallographic flat origamis, Memoirs of the Faculty of Science. Kyushu University Ser A 1988; 42: 153-157. https://doi.org/10.2206/kyushumfs.42.153.

[48] Peng R, Chen Y. The metamaterial generated from rigid-origami pattern. The 6th International Meeting on Origami in Science, Mathematics and Education, Tokyo, Japan, 2014.

[49] Hull TC. Counting mountain-valley assignments for flat folds. Ars Combinatoria 2003; 67:175-188.

[50] Hull TC. Project origami: activities for exploring mathematics, A K Peter/CRC Press, Wellesley, MA, 2006.

[51] Evans TA, Lang RJ, Magleby SP, Howell LL. Rigidly foldable origami twists. In: Origami 6; 2015, p. 119-130.

[52] Feng H, Peng R, Zang S, Ma J, Chen Y. Rigid foldability and mountain-valley crease assignments of square-twist origami pattern. Mech Mach Theory 2020; 103947. https://doi.org/10.1016/j.mechmachtheory.2020.103947.

[53] Kamrava S, Ghosh R, Xiong J, Felton SM, Vaziri A. Origami-equivalent compliant mechanism, Appl Phys Lett 2019; 115: 171904. https://doi.org/10.1063/1.5115790.

[54] Wang LC, Song WL, Zhang YJ, Qu MJ, Zhao Z, Chen M, Yang Y, Chen H, Fang D. Active reconfigurable tristable square-twist origami. Adv Funct Mater 2020; 1909087. https://doi.org/10.1002/adfm.201909087.

[55] Wang LC, Song WL, Fang D. Twistable Origami and Kirigami: from Structure-guided smartness to mechanical energy storage. ACS Appl Mater Interfaces 2019; 11: 3450–3458. https://doi.org/10.1021/acsami.8b17776.

[56] Edmondson BJ, Lang RJ, Morgan MR, Magleby SP, Howell LL. Thick rigidly foldable structures realized by an offset panel. In: Origami 6; 2015, p. 149-161.

[57] Hull TC, Urbanski MT. Rigid foldability of the augmented square twist. In: Origami 7; 2018, p. 533-544.

[58] Liu K, Paulino GH. Nonlinear mechanics of non-rigid origami: an efficient computational approach. Proc R Soc A 2017; 473: 20170348. http://dx.doi.org/10.1098/rspa.2017.0348.

[59] Schenk M, Guest SD. Origami Folding: A Structural Engineering Approach. In: Origami 5; 2011, p. 291-303.

[60] Lu G, Yu TX. Energy absorption of structures and materials. Cambridge, UK: CRC-Woodhead; 2003.